METEOROLOGICAL APPLICATIONS
Meteorol. Appl. **22**: 599–609 (2015)
Published online 18 February 2015 in Wiley Online Library
(wileyonlinelibrary.com) DOI: 10.1002/met.1494

RMetS
Royal Meteorological Society

Atmospheric thickness and vertical structure properties in wintertime precipitation events from microwave radiometer, radiosonde and wind profiler observations

Dong-Kyun Kim and Dong-In Lee*

Department of Environmental Atmospheric Sciences, Pukyong National University, Busan, Korea

ABSTRACT: With a focus on the properties of atmospheric thickness, temporal variations of various atmospheric quantities at isobaric levels measured and retrieved from microwave radiometer (MWR) and radiosonde soundings were investigated for precipitation events during the winter of 2011 near Seoul, Korea. Wind profiler analyses were performed additionally for examining the returned radar power signal and Doppler velocity characteristics of the vertical structure. It was found that there exists a lead period of 9 to 12 h that shows little change (almost no increase) in the 1000–850 hPa thickness before precipitation. Between snow and rain events, thermodynamic characteristics were similar at lower levels but were noticeably different at upper levels, showing their dependence on the cloud-top height and updraft intensity. Higher correlation in thickness and temperature between the MWR and radiosonde data was found at lower levels than upper, suggesting that the lead period of the 1000–850 hPa thickness as shown by the MWR is reliable in this study. The vertical structure and precipitation properties analysed from wind profiler observations showed close agreement with MWR retrievals of precipitable water vapour and liquid water content, indicating the effectiveness of the wind profiler as a complementary tool in MWR studies.

KEY WORDS atmospheric thickness; thermodynamics; microwave radiometer; vertical structure; wind profiler

Received 30 June 2014; Revised 28 September 2014; Accepted 7 November 2014

1. Introduction

Over the past decade, meteorological applications of the microwave radiometer (MWR) have remarkably increased as the MWR has proved its effectiveness in various fields relative to conventional radiosonde observations (RAOBs) (Güldner and Spänkuch, 1999, 2001; Löhnert *et al.*, 2004, 2009; Cimini *et al.*, 2011, 2014; Ware *et al.*, 2013; Xu *et al.*, 2014). Automated, continuous thermodynamic profiling of the MWR up to 10 km above ground level (AGL) at a high time resolution is critical for monitoring real-time thermodynamic states as well as for improving short-range forecasts of rapidly changing weather phenomena by assimilating MWR retrievals into models. Many applications that use the MWR have been documented in previous studies on boundary layer thermodynamics, clouds and precipitation (Güldner and Spänkuch, 2001; Knupp *et al.*, 2009; Campos *et al.*, 2014; Serke *et al.*, 2014), retrieval of precipitable water vapour (PWV) and liquid water path (LWP) in comparison with those derived from GPS and RAOBs (Liou *et al.*, 2001; Van Baelen *et al.*, 2005), and convective weather nowcasts (MacDonald *et al.*, 2002; Chan, 2009; Madhulatha *et al.*, 2013; Venkat Ratnam *et al.*, 2013; Cimini *et al.*, 2014). The MWR can perform well with sufficient accuracy under both clear and cloudy sky and precipitating conditions (Chan, 2009; Ware *et al.*, 2013; Campos *et al.*, 2014; Serke *et al.*, 2014; Xu *et al.*, 2014), but retrieval errors or biases may occur in cases of heavy rain associated with rain contamination although there is a blower system that blows ice or liquid particles away from the radiometer radome (Chan, 2009). Recently, in order to reduce such intrinsic errors of retrievals, Xu *et al.* (2014) used MWR temperature and vapour density profiles retrieved from an off-zenith direction (15° elevation) during precipitation and indicated that they generally show higher accuracy compared with zenith observations. For light to moderate rain, Liu *et al.* (2001) estimated rainfall rates based on a positive relationship between MWR brightness temperatures and precipitation intensities and showed good agreement between the estimated rainfall rates and the observed ones.

MWR studies combined with other active remote sensors such as radar, wind profiler and ceilometer have been conducted increasingly in recent years, enhancing their incorporated observation abilities to examine in more detail the dynamic and thermodynamic properties of various atmospheric phenomena (Westwater *et al.*, 1983, 2003; Löhnert *et al.*, 2004, 2011; Bianco *et al.*, 2005; Kneifel *et al.*, 2010; Spänkuch *et al.*, 2011; Campos *et al.,* 2014). Gaffard *et al.* (2008) investigated the boundary layer structure and thermodynamic properties using various ground-based remote sensors including a MWR and a wind profiler and showed a high correlation between the vertical velocities observed from the wind profiler and low-level thermal properties from the MWR. Campos *et al.* (2014) also examined in detail the characteristics of mixed phase particles in winter clouds using the measurements of a MWR and a wind profiler, which were found to agree. Developing indices for convective instability and wind gust from MWR profiles was attempted by comparison with those derived from both radiosonde and wind profiler observations, indicating their potential to be a precursor to short-term forecasts of severe weather (Chan, 2009; Madhulatha *et al.*, 2013; Venkat Ratnam *et al.*, 2013; Cimini

* Correspondence: Dong-In Lee, Department of Environmental Atmospheric Sciences, Pukyong National University, Busan, Korea. E-mail: leedi@pknu.ac.kr

et al., 2014). Thresholds of atmospheric thickness have also been studied (Keeter and Cline, 1991; Heppner, 1992) as a means to predict and determine precipitation types. Keeter and Cline (1991) noted that relative to the 1000–500 hPa thickness, low-level thicknesses of 1000–850 hPa and 1000–700 hPa are more effective for differentiating precipitation types as well as for forecasting maximum surface temperatures since they are more sensitive to low-level thermal structures. In-depth studies of the time series properties of thickness using both the MWR and radiosonde data on precipitating events have been limited. With a focus on the characteristics of low-level thickness in particular, this study presents the results on vertical structure and thermodynamic properties prior to and during precipitation, in combination with wind profiler observations.

2. Cases and instruments

2.1. Cases

Two snow events on 10–11 and 13 January 2011 and a rain event on 26–27 February 2011 were selected from winter observations between 2 January 2011 and 2 March 2011. On 10 January 2011, widespread snow clouds oriented northeast–southwest were observed over the Yellow Sea. Figure 1(a) shows that a surface low pressure existed over the Yellow Sea, west of the Seoul area at 0300 UTC on 11 January. With the surface low pressure moving towards the east, the clouds brought mild snowfall to the Seoul area during daytime, recording a total of 2.8 cm for a duration of about 12 h. On 13 January 2011, snow clouds similar to that of the former event moved to the same area and produced little snowfall during night time. Before snow began, southerly and southwesterly winds were dominant near the surface in both the events. In the 10–11 January event, with a continuous drop in surface pressure, a cyclonic wind change from south to northeast with time was observed at the surface, which indicates a frontal passage accompanied by the surface low pressure. A minimum surface pressure of 1015 hPa was reached at nearly 0500 UTC on 11 January, i.e. almost when the second snowfall occurred (Line 2 in Figure 2(a)), whereas the cyclonic wind change was not observed in the 13 January event. Surface winds on the 10–11 January event were relatively weaker than those on the 13 January event. The third event examined was a rainfall event on 26–27 February, developed with low pressure passage. The rainfall system had a stratiform structure showing a pronounced bright band near the ∼2 km AGL melting level that is common in late Korean winter with surface temperatures above 0 °C. Rainfall lasted for approximately 10 h with surface rainfall rates up to 8 mm h^{-1}.

2.2. Instruments and method

The MWR used in this study is a 35 channel passive radiometer (MP-3000A) manufactured by the Radiometrics Corporation (USA). During the winter observation period of 2 months, the MWR was operated with radiosonde launches at the Incheon observatory, which is about 30 km west of Seoul, and a 1290 MHz wind profiler was located at the Munsan observatory about 35 km northwest of Seoul (see Figure 1(b)). The distance between the two observatories is about 50 km. The MWR observes atmospheric microwave emission in a water vapour band of 21 frequencies ranging from 22 to 30 GHz and an oxygen band of 14 frequencies ranging from 51 to 59 GHz. Associated with a broadening effect by atmospheric pressure, the water vapour band is used to retrieve water vapour profiles because water vapour absorbs and emits microwave radiation strongly in this band. The frequencies in the oxygen resonance band are used to retrieve temperature profiles. Both bands include liquid water profile information (Solheim *et al.*, 1998; Knupp *et al.*, 2009; Ware *et al.*, 2013; Campos *et al.*, 2014; Serke *et al.*, 2014). Most of the temperature information is obtained from the lower layers because the atmosphere is optically opaque near 60 GHz and the rest of the information is from the upper layers because the atmospheric transparency increases away from the 60 GHz line (Kneifel *et al.*, 2010). MWR temperature, humidity and liquid water profile retrievals are recorded in the data files as a function of height AGL. By using the MWR temperature data with levels, the atmospheric thickness directly proportional to layer mean temperature between neighbouring two levels is derived using a hypsometric equation and interpolation. The calculated atmospheric thicknesses are compared with those from RAOBs derived in the same way and their temporal properties are analysed in more detail in this study.

For retrieving vertical profiles of the MWR variables, brightness temperatures observed at each channel, *in situ* surface temperature, relative humidity, pressure and cloud base temperature from an infrared thermometer are used as input data to a neural network algorithm, trained beforehand with historical radiosonde soundings from a launch site near the MWR site. As integrated quantities, PWV and LWP are also retrieved from the neural network. For more information about the algorithm, see Solheim

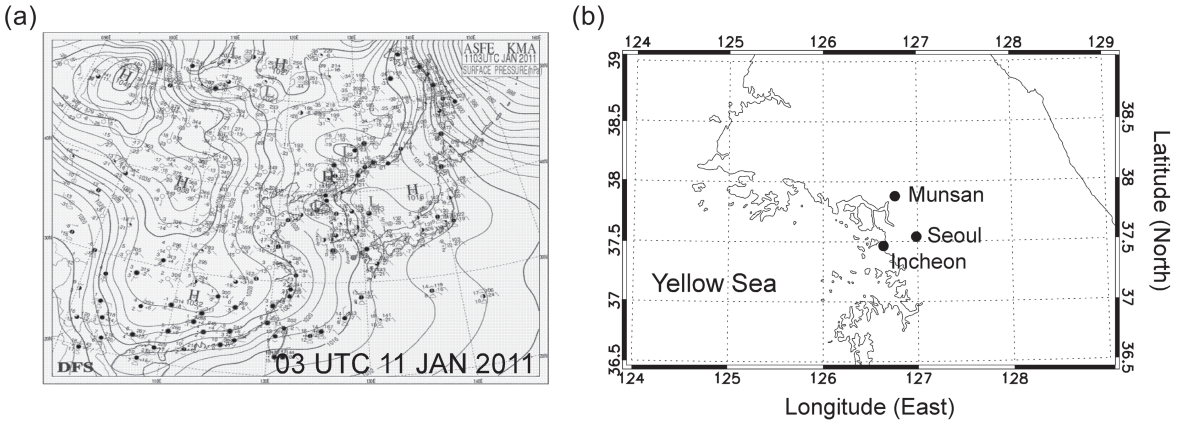

Figure 1. (a) Surface pressure (hPa) chart at 0300 UTC on 11 January and (b) geographic map showing locations of the Munsan and Incheon observatories mentioned in the text.

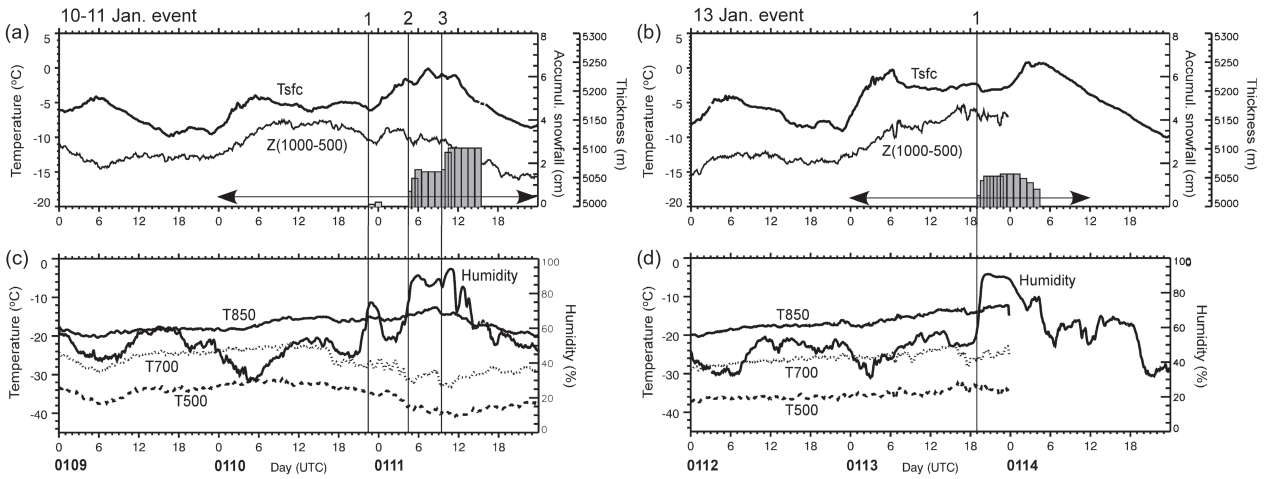

Figure 2. Time series of (a) Z(1000–500) (m, solid line), Tsfc (°C, dashed line) and accumulated snowfall (cm, grey bar) in intervals of 30 min or 1 h, (b) T850 (°C, long dash line), T700 (°C, dotted line), T500 (°C, short dash line) and relative humidity (%, solid line) in the 10–11 January event. Time series in the right two panels are the same as (a) and (b) but for the 13 January event. The vertical lines indicate the times of snowfall occurrence. The horizontal arrows on *x*-axis in (a) and (c) indicate the analysis periods of PWV and LWP in Figure 3. Time is in UTC. For local standard time (LST), UTC + 9 h.

et al. (1998). Vertical resolution of retrieved profiles is smallest at 50 m from the ground to 500 m AGL. It decreases to 100 m between 500 m and 2 km AGL and to 250 m between 2 and 10 km AGL. Time resolution of sampling vertical profiles is around 3–4 min. Radiosondes are launched at the MWR site for comparison with the MWR measurements. Vaisala RS92-SGPW radiosondes using water-activated battery are used and uncertainties in temperature and humidity sounding are 0.5 °C and 5%, respectively. Radiosonde launches are made two times *per* day and increased to four times *per* day in case of precipitation.

For a more detailed examination of the vertical structure of the snow and rain clouds, wind profiler observations of signal-to-noise ratio (SNR), Doppler velocity, spectral width and winds were analysed. The wind profiler is a vertically pointing Doppler radar that receives both backscattered echoes from hydrometeors and irregularities in refractive indices by turbulence in the upper air. The profiler used is a 1290 MHz wind profiler manufactured by Degreane (France). At this frequency, the wind profiler is more sensitive to Rayleigh echoes from snow particles or raindrops. A five-beam sequence is used for calculating winds. Time and height resolution for high modes are 10 min and 165 m AGL, respectively. The maximum observation height is 9.95 km AGL. Details of the parameters of the profiler are shown in Table 1.

Table 1. Operational parameters of the 1290 MHz wind profiler (high mode).

Parameters	
Wavelength	23 cm
Pulse repetition frequency	20 000
Inter pulse period	1000 μs
Pulse width	80 μs
Number of coherent integrations	100
Number of spectral averages	50
Number of Fast Fourier Transform (FFT) points	128
Transmitted power	3500 W
Number of range gates	59

3. Results

3.1. Properties of time series in the snow events

Temporal variations in temperature, relative humidity (RH) and 1000–500 hPa thickness [Z(1000–500)] during the snow events are shown in Figure 2. The surface temperature, RH and accumulated snowfall were observed by sensors on the ground, and upper-level temperatures were observed by the MWR. The first snowfall was recorded at 2230 UTC on 10 January 2011 although the amount of snowfall was not much. Following this, there were two more occurrences of snowfall. In the left panels of Figure 2, three vertical lines indicate the time (2230 UTC 10 January, 0430 UTC 11 January, 0930 UTC 11 January) at which snowfall occurred in the 10–11 January event. In Figure 2(a) the snowfall shown by the grey colour bar is accumulated snowfall amount recorded at 30 min or 1 h interval. In Figure 2(b), the steady increase in temperature at 850 hPa (T850) up to Line 3 is seen. Also, the decreasing trend in Z(1000–500) and temperatures at 700 hPa (T700) and 500 hPa (T500) is clearly observed from around 1000 UTC on 10 January, about 12 h before Line 1. This is due to cold air advection driven by an approaching upper 500 hPa trough during this period. T500 and T700 reached a minimum of −41 and −34 °C at around 1100 UTC on 11 January, respectively, which is about 6 h after the surface low pressure reached a minimum at ∼0500 UTC on 11 January near Line 2 when the surface low pressure was centred over the Seoul area (not shown). Generally, a surface low pressure precedes an upper level trough associated with downward motion that helps to strengthen the convergence and positive vorticity over the surface low. It is noted that the ongoing decrease in Z(1000–500) despite the increasing trend of T500 and T700 from ∼1100 UTC to 2400 UTC on 11 January is attributed more to the decrease in both Tsfc and T850. In Figure 2(b), with the sharp increase in Tsfc and RH, the more notable increase in T850 from Line 1 to around Line 3 is related to strengthened warm moist airflow by southwesterly winds at low levels. The setting of low-level warm air below upper cold air advection (i.e. the decrease in T700 and T500) increased the conditional instability in the area, making a favourable condition for snowfall occurrences. Tsfc, T850 and RH decreased from ∼1100 UTC on

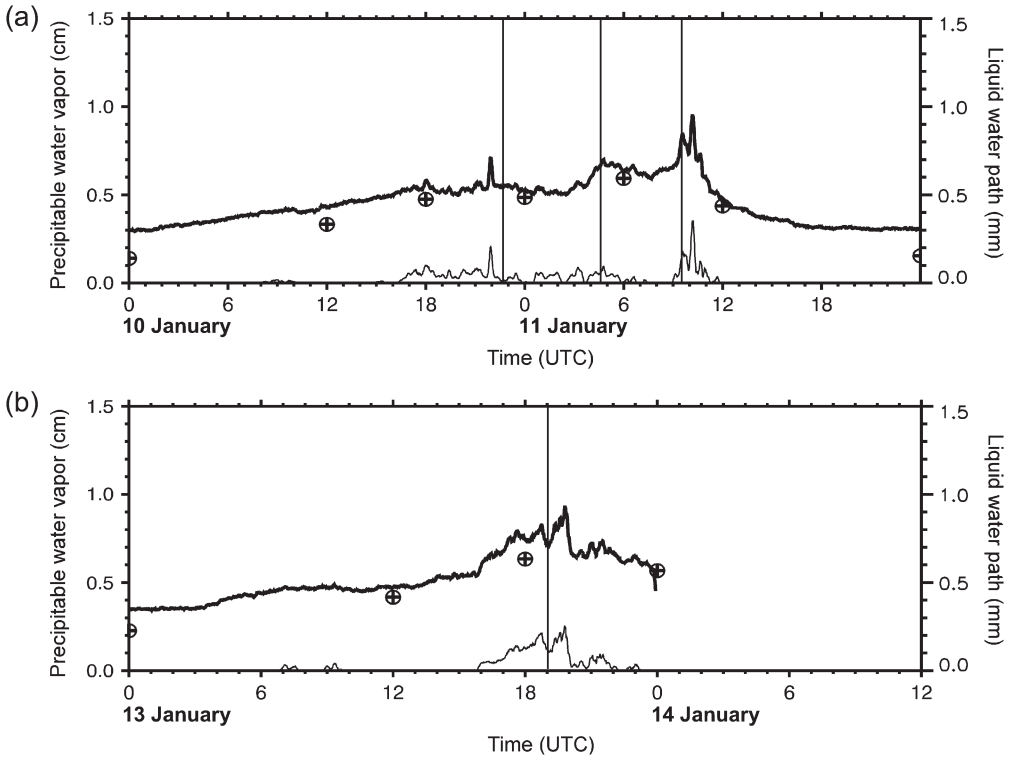

Figure 3. (a) PWV (mm, thick solid line) and LWP (mm, thin solid line) from the MWR and PWV (mm, circle with cross) from RAOBs for the 10–11 January event. (b) Same as (a) but for the 13 January event. The vertical lines indicate the times of snowfall occurrence (see Figure 2).

11 January as the surface low pressure centre moved away from the MWR site.

For the 13 January event in Figure 2(c), it is found that Tsfc is relatively warmer with larger Z(1000–500) before 1900 UTC on 13 January when the first snowfall occurred (Line 1), compared to the 10–11 January event (Figure 2(a)). Surface winds are relatively stronger than those in the 10–11 January event and a continuous drop of surface pressure with time was not observed (not shown). Thus, a margin area of the surface low pressure system might be observed by the MWR, producing less snowfall of 1.5 cm. In Figure 2(d), T850, T700 and T500 showed a steady increase to Line 1 although T700 showed a slight decrease in about 3 h before Line 1. This is well contrasted with the decreasing trend in T700 and T500 in the 10–11 January event. Unfortunately, MWR measurements were not available after 2300 UTC on 13 January.

Figure 3 shows the time series of MWR PWV (MPWV) and MWR LWP (MLWP) in the two events for the time periods indicated by the horizontal arrows on *x*-axis of Figure 2(a) and (c), respectively. Overall, MPWV values are in close agreement with PWV (RPWV) derived from RAOBs in both the events. It is noted that MPWV is more positively correlated with T850 than T700 and T500, indicating that MPWV is more affected by low-level thermal properties than upper-level ones. The peak values of MPWV and MLWP are almost aligned with the vertical lines in Figure 3(a) and (b). There was no correlation between MPWV and Z(1000–500) in the 10–11 January event. Whereas, the MPWV is weakly dependent on Z(1000–500) before the snow begins in the 13 January event when there was no drop in upper air temperatures.

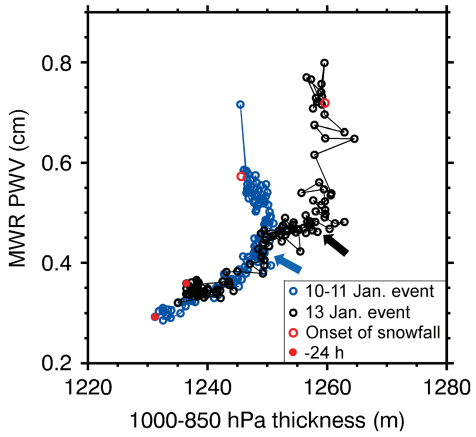

Figure 4. Scatter plots between MPWV (cm) and Z(1000–850) (m) for the two snow events. Data points at snowfall onset and 24 h prior are indicated. Blue and black data points are from the 10–11 and 13 January events, respectively. The symbols are annotated in the box at the right lower corner. Each arrow indicates the approximate maximum curvature point.

3.2. MWR thickness characteristics of the snow events

Figure 4 shows scatter plots of MPWV and 1000–850 hPa thicknesses [Z(1000–850)] for the two snow events. Data for 24 h before the start of snowfall were used in the scatter plots. Overall, there is a positive relation between MPWV and Z(1000–850) for both the events. Interestingly, the Z(1000–850) values are converged roughly at ~1250 m for the 10–11 January event and at ~1260 m for the 13 January event, respectively, both producing the shape of a large curve. The arrows indicate the

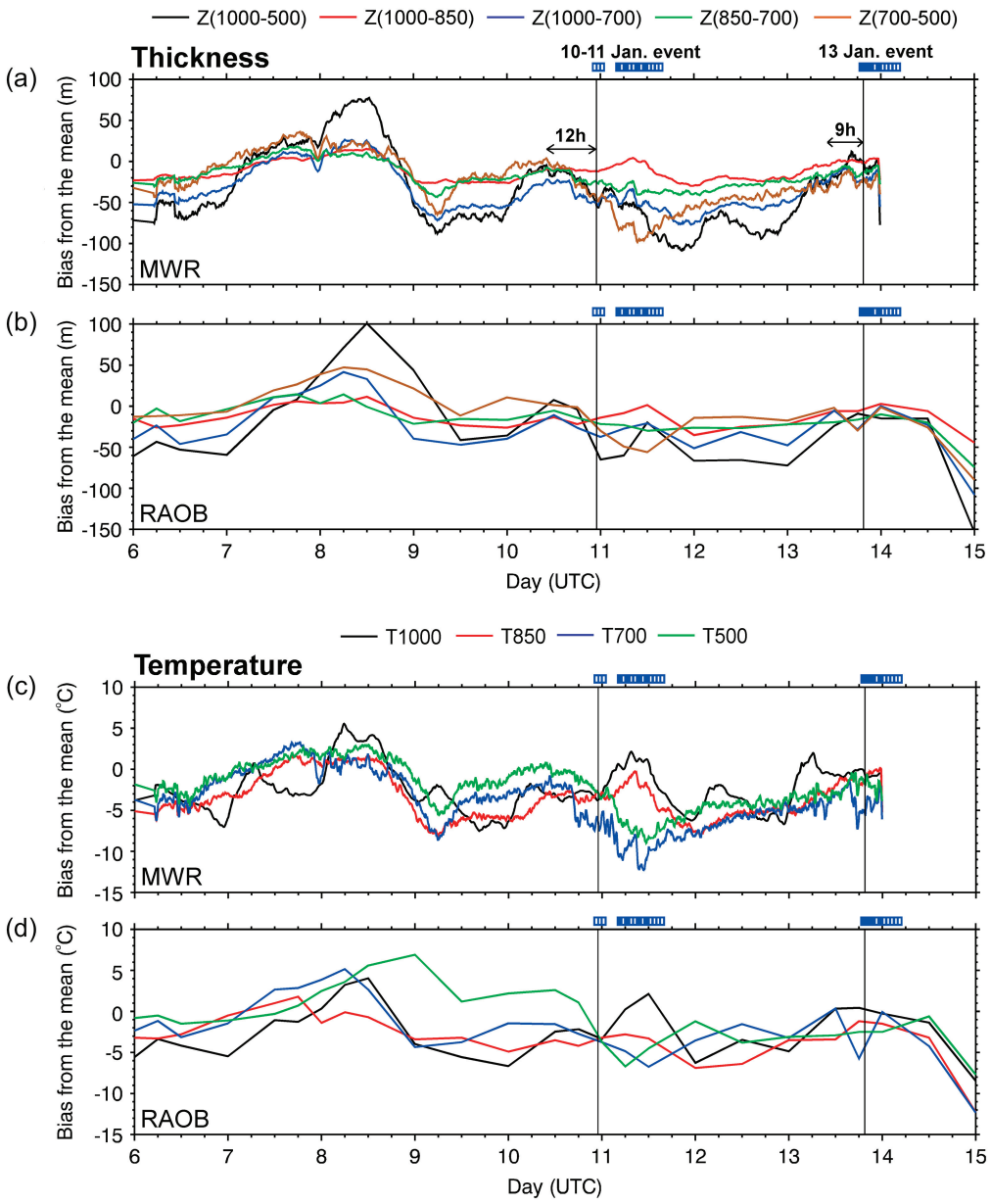

Figure 5. (a) Time series of thickness bias from the mean, which is derived from the MWR and (b) from RAOBs and (c) time series of temperature bias from the mean, which is observed from the MWR and (d) from RAOBs in different isobaric levels and layers. The blue rectangles on the top of each panel represent the periods of snowfall. The vertical lines indicate the times of the first snowfall for each event (i.e. 2230 UTC on 11 January and 1900 UTC on 13 January). In (a), the horizontal arrows indicate the lead periods of 12 and 9 h in each event based on the Z(1000–850) time series in red. See text for more detail.

maximum curvature points. All the Z(1000–850) values are below a critical threshold of 1280 m for forecasting snowfall, as proposed by Heppner (1992). The relatively larger Z(1000–850) values in the 13 January event indicate that the air below ~1.5 km AGL is relatively warmer than that in the 10–11 January event, consistent with the higher Tsfc and T850, as shown in Figure 2(c) and (d).

From the maximum curvature points in Figure 4, it is found that there were lead periods of about 12 and 9 h before the snow begins in the 10–11 and 13 January events, respectively, which show little change in Z(1000–850) relative to that before the lead periods. That is, the mean virtual temperature in the 1000–850 hPa layer starts becoming constant from 12 and 9 h before the snow event in this study. The curve shape was also found in the scatter plot of Z(1000–500) and MPWV (not shown here) but is not marked owing to the decreasing Z(1000–500) as shown in Figure 2(b). Massie and Rose (1997) noted that Z(1000–850) has a strong linear relation with surface temperature. Related to this, the relatively uniform change of Z(1000–850) is more easily found from the time series of Tsfc and T850 in Figure 2(a) and (b) that shows similar variations from about 10 h before Line 1. Although the lead periods are rough estimates and can differ from case to case, it is noted that the MWR could resolve such a minimal change in Z(1000–850), which cannot be resolved by RAOBs.

3.3. MWR validation with RAOB

Figure 5 shows the time series of thickness and temperature biases from the mean, which enables one to better compare them

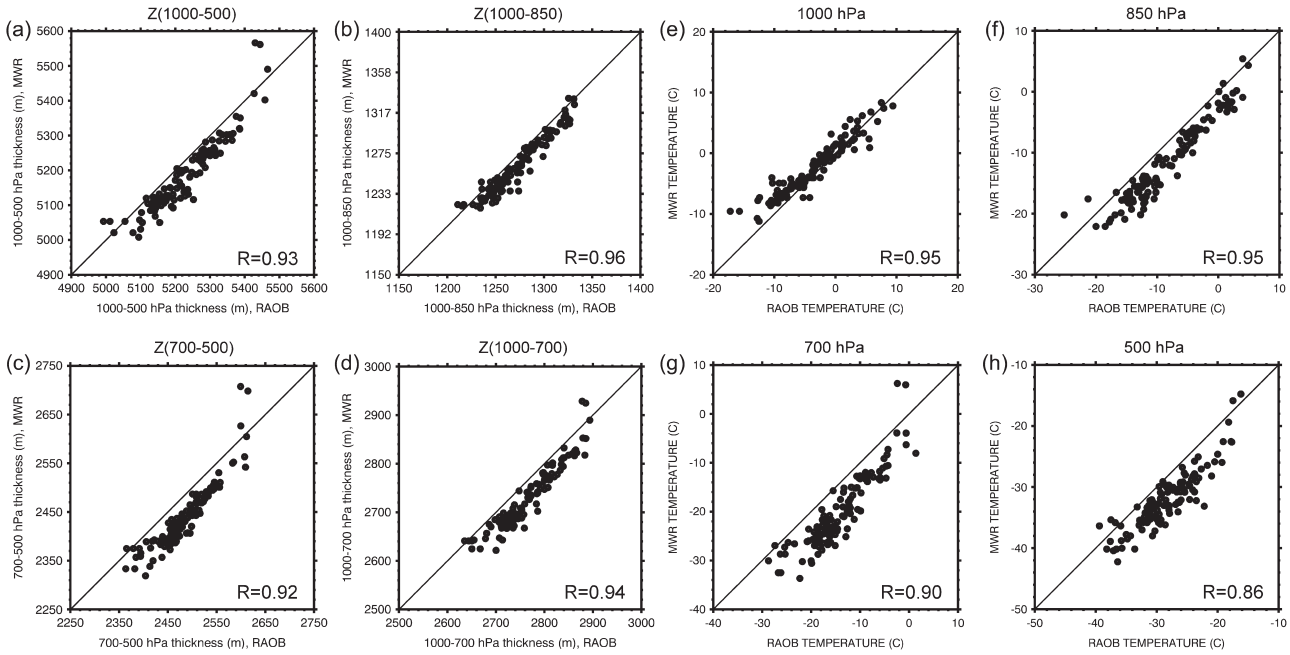

Figure 6. Scatter plots of thicknesses in the left four panels (a, b, c, d) between the MWR and RAOBs at four different pressure layers and temperatures in the right four panels (e, f, g, h) between the MWR and RAOBs at 1000, 850, 700 and 500 hPa levels, respectively, during the observation period.

between different isobaric levels. Overall, the thicknesses and temperatures from the MWR are in good agreement with those from RAOBs observed at 6 and 12 h intervals, showing similar temporal variations. In Figure 5(a), relatively more uniform changes in Z(1000–850) regarding the lead periods of 12 and 9 h as noted in the previous section are clearly seen before the snow begins in each event (see the horizontal arrows). This feature of Z(1000–850) is well contrasted to all other thicknesses that showed larger variations during the same period. In the 10–11 January event, all the thicknesses except for Z(1000–850) showed a decreasing trend from about 12 h before snow begins. Similar findings are observed from 1200 UTC on 10 January in the RAOB thicknesses in Figure 5(b). The vertical depth of the biases in the thickness comparisons is largest in Z(1000–500) and smallest in Z(1000–850). As noted in Section 3.1, the drop of T700 and T500 is well revealed in Figure 5(c) in contrast to the increase of Tsfc and T850 after the snow begins in the 10–11 January event. The RAOB temperatures also showed similar variations in this period (Figure 5(d)).

In addition to the time series comparisons, their scatter plots were also made to examine the correlation with height between MWR and RAOBs. In Figure 6, there were high correlation co-efficients over 0.9 on all the left four panels showing some biases to the RAOB thicknesses. The highest correlation ($R = 0.96$) was found in Z(1000–850) in Figure 6(b). The lowest correlation with the largest bias of ∼50 m to RAOB was in Z(700–500) that covers the upper 1000–500 hPa layer. The decreased correlations in Z(700–500) and Z(1000–500) with more scatter are probably due to the drift of radiosondes with height. Particularly, the relatively high correlations in Z(1000–850) and Z(1000–700) are probably because they account for thermal properties at lower levels at more fine vertical resolutions of the MWR, as introduced in Section 2.2. The temperature comparisons in the right four panels show high correlation co-efficients over 0.86. The highest correlation ($R = 0.95$) was found at 1000 hPa level in Figure 6(e). As discussed above, the correlations in the temperature comparisons also tended to decrease with height, showing more scatter. Except for the 1000 hPa level, there was a mean bias of 3–5 °C to the RAOB temperatures.

3.4. Combined MWR and wind profiler analysis of the 10–11 January snow event

Figure 7 shows time-height sections of temperature, RH and water vapour density from the MWR and SNR from the wind profiler for the 10–11 January event. The returned power signals backscattered from snow particles show that the SNR is proportional to snowfall intensities. In Figure 7(a), a temperature decrease due to the approach of upper cold trough is clearly visible at 2–4 km AGL from 1600 UTC on 11 January. The coldest air temperature reaching 230 K is found at 3.5–4 km AGL near Lines 2 and 3 when the snowfall occurred. In Figure 7(b), the saturation (100%) region of RH started to appear at ∼2 km AGL from 1630 UTC on 11 January. The RH was ∼90% near the surface at Line 1. The saturation region was found to gradually lower and almost touch the ground level at Lines 2 and 3 when relatively stronger snowfall was observed (see also Figure 2(a)) with high vapour densities over 3.0 g m^{-3} in Figure 7(c).

In Figure 7(d), high SNR values over 30 dB were observed below ∼1 km AGL, indicating the presence of relatively large snow particles. The high SNR values were well matched with the regions of 100% RH and high water vapour densities along Lines 2 and 3. The high SNR over 40 dB around Line 1 was not physically consistent with the light snowfall observed over the MWR site. This is probably due to the spatial inhomogeneity related to the distance between the MWR and the profiler. In practice, it was found that the profiler observed a localized, strong echo area of the clouds as it passes overhead during this period. One important thing is that the upper boundary of SNR at a minimum of ∼5 dB is very close to the isoline of 100% RH at ∼2.5 km AGL during the snowfall (around Lines 2 and 3 in Figure 7(b)), indicating that the snow clouds were shallow. Since the profiler is not sensitive to cloud droplets and tiny ices, the

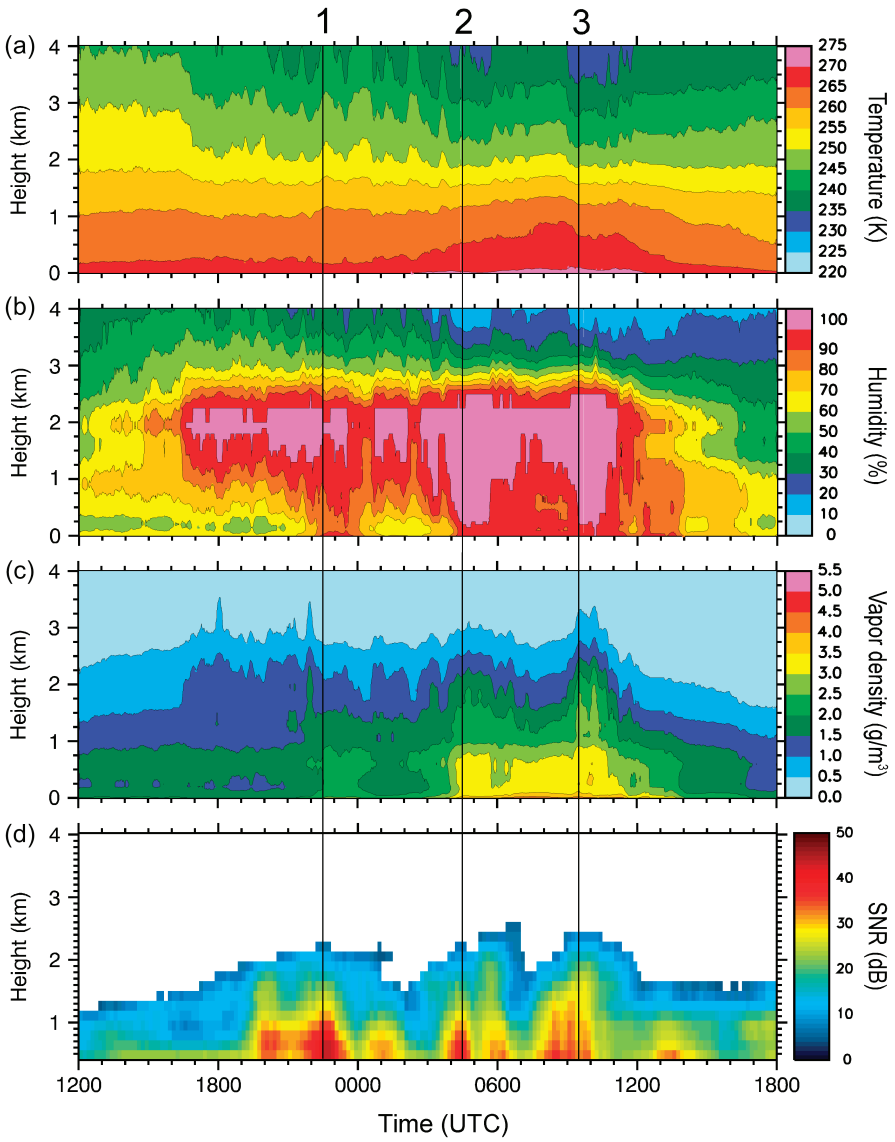

Figure 7. Time-height sections of (a) temperature, (b) RH, (c) vapour density observed from the MWR and (d) SNR from the wind profiler from 1200 UTC on 10 January to 1800 UTC on 11 January. The three vertical lines indicate the times of snowfall occurrence as shown in the left panels of Figure 2.

cloud top height is usually higher than that determined from the SNR minimum of ∼5 dB in this study. With the information of the 100% RH heights, the cloud top height would be ∼3 km AGL.

3.5. Time series properties of thickness and temperature in the rain event

In Figure 8(a) and (b), a similar time series as in Figure 2 for the rain event on 26–27 February 2011 is shown. In contrast to the snow events, a sharp increase in T700, T500 and Z(1000–500) is clearly seen in ∼3 h before the rain starts at ∼1930 UTC (vertical line) in Figure 8(b), which indicates that the rain system is basically warmer than the environment. The time series showed no large variations during the rain period from 1930 UTC on 26 February to 0930 UTC on 27 February. From the upper boundaries of the SNR minimum and 100% RH, a cloud top height of 7–8 km AGL is approximated in this event. It is shown in Figure 8(c) that there is a relatively larger difference between the MPWV and RPWV during the rain period, probably due to rain contamination (Xu *et al.*, 2014). Similar to the temperatures in Figure 8(b), MPWV showed a sharp increase in ∼3 h before the rain and its slope of increase was much steeper than that in the snow events. The MPWV maximum is almost 4 times and the MLWP maximum is 15 times larger than those in the 10–11 January event, respectively, indicating that liquid water amounts are more abundant in this rain event. The MLWP is almost proportional to the surface rain rates (R) in Figure 8(a) and the MPWV is positively correlated with T700, T500 and Z(1000–500) in contrast to that in the snow events.

Figure 9 shows the same scatter plots as in Figure 4 but for the rain event with data points of −24 h before the start of rainfall. In Figure 9(a), a notable curvature is found similar to those in the snow events. Z(1000–850) is almost converged at ∼1320 m. All the Z(1000–850) values are above the critical value of 1280 m for snow occurrence (Heppner, 1992). In this rain event, the lead time period that shows almost no change in Z(1000–850) before the rain begins is ∼11 h. In Figure 9(b), Z(1000–500) is largely bent at ∼5400 m but the curve shape is less notable compared

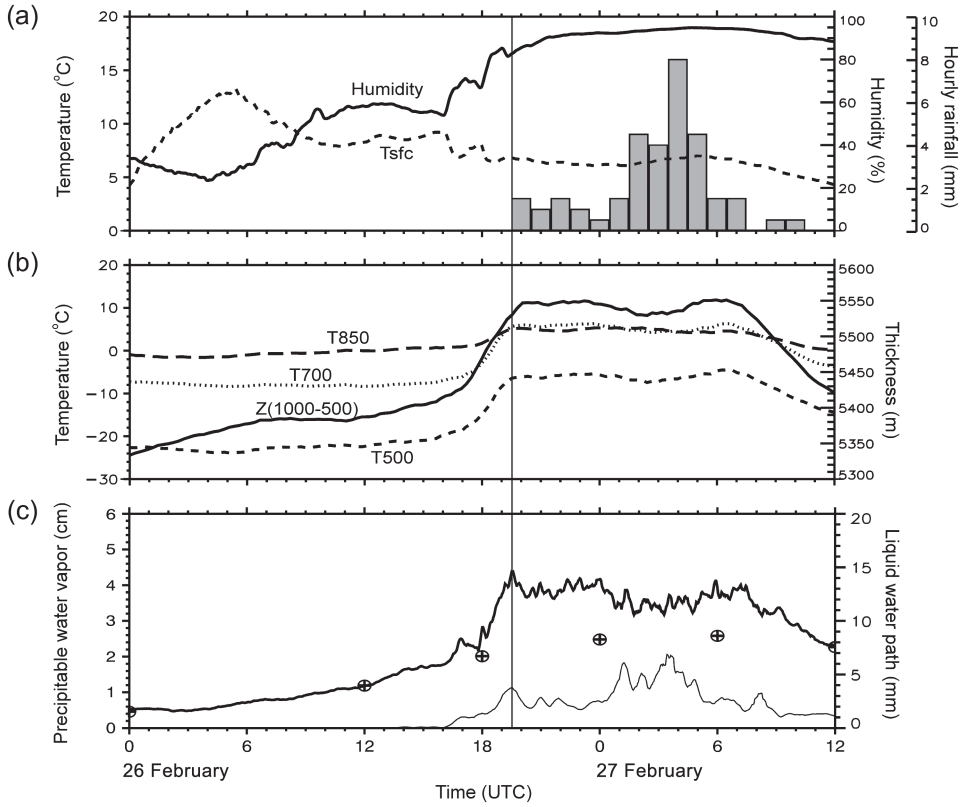

Figure 8. Time series of (a) relative humidity (%, solid line), Tsfc (°C, dashed line) and hourly rainfall (mm, grey bar), (b) T850 (°C, long dash line), T700 (°C, dotted line), T500 (°C, short dash line) and Z(1000–500) (m, solid line) and (c) PWV (mm, thick solid line) and LWP (mm, thin solid line) from the MWR and PWV (mm, circle with cross) from RAOBs for the 26–27 February rain event. The vertical line indicates the start time of rainfall (1930 UTC on 26 February).

to that in Z(1000–850), rather making a more linear shape. This is because Z(1000–500) is relatively more influenced by thermodynamic flows at upper levels than Z(1000–850) in this study.

3.6. Combined MWR and wind profiler analysis of the rain event

In about 1.5 h before the rain begins, a rapid increase in all-level temperatures is shown up to 10 km AGL in Figure 10(a), indicating a larger vertical extent of the rain clouds. A gradual decrease of cloud base heights appeared from ∼6 km AGL at 0700 UTC on 26 February, as seen in Figure 10(b). At around the start time of rainfall (vertical line), the cloud base heights were ∼1 km AGL with some fluctuations and almost touched the ground from 0130 to 0500 UTC on 27 February when the surface R increased up to 8 mm h^{-1} (Figure 8(a)) with the large liquid water content over 0.5 g m^{-3} (Figure 10(c)).

In Figure 11(a), a pronounced bright band at ∼2 km AGL starts to appear from ∼1800 UTC in ∼1.5 h before the rain. The temporal mismatch is due to the distance between the MWR and the profiler. It appears that the profiler, ∼30 km north of the MWR site, could observe the rain system about 1.5 h earlier as the system was moving from the northwest, nearer to the profiler site than the MWR site. The bright band height that is marked by a rapid increase of Doppler velocities from snow to rain in Figure 11(b) shows a gradual rise with time and is highest ∼0400 UTC on 27 February. The higher bright band during the 0130–0500 UTC on 27 February period is related to warm southerly and southeasterly winds observed at low levels (see Figure 11(d)). The surface R is relatively larger in this period (Figure 8(a)). The larger Doppler velocities of −6 to −7 m s^{-1} (negative downward) below the melting layer in Figure 11(b) indicate a presence of larger raindrops during this high R period. It is found that the surface R from 1930 UTC on 26 February to 1030 UTC on 27 February in Figure 8(a) tended to be positively correlated with the height of the bright band.

In Figure 11(c), the largest spectral widths reaching 4 m s^{-1} in the melting layer were observed particularly during the period 0130–0500 UTC on 27 February, showing the large surface R. The increase in spectral widths is primarily due to wider size and fall velocity distributions of mixed phase particles by aggregation and breakup processes in the vicinity of the melting layer. Large raindrops melted from large snow aggregates right above the melting layer contributed to increasing the surface R during this period. The spectral widths also tended to increase with wind speeds above the melting layer in Figure 11(c) and (d). It is probably because the observed Doppler spectra with mean fall velocities of 1–2 m s^{-1} can be more affected by horizontal winds in ice regions than by those in rain regions. Less than ∼2 km AGL in Figure 11(d), irregular, weak winds were observed during weak rain until ∼0100 UTC 27 February. As the surface R increased after 0130 UTC on 27 February, southwesterly winds prevailed, showing a notable veer with height. In particular, with near-surface cloud base heights and liquid water contents of 0.1 ∼ 0.3 g m^{-3} up to ∼300 m AGL in Figure 10(b) and (c), the SNR values greater than 30 dB to this level with the almost zero Doppler velocities and low spectral widths indicate that the occurrence of fog is very likely near the surface from 1700 UTC on 27 February to 0000 UTC on 28 February.

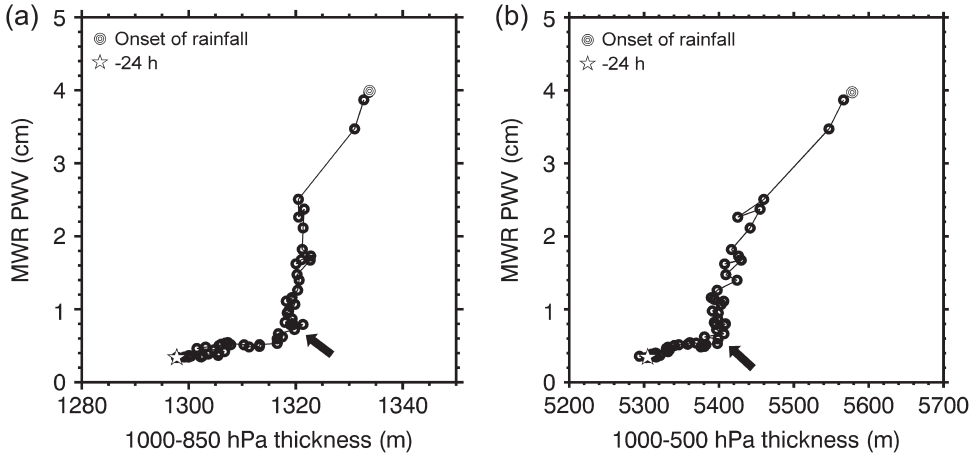

Figure 9. Scatter plots of (a) MPWV (cm) and Z(1000–850) (m) and (b) MPWV (cm) and Z(1000–500) (m) for the 26–27 February rain event. Data points at rainfall onset and 24 h prior are shown. The symbols used are annotated in the left upper corner. The black arrows indicate the approximate maximum curvature points.

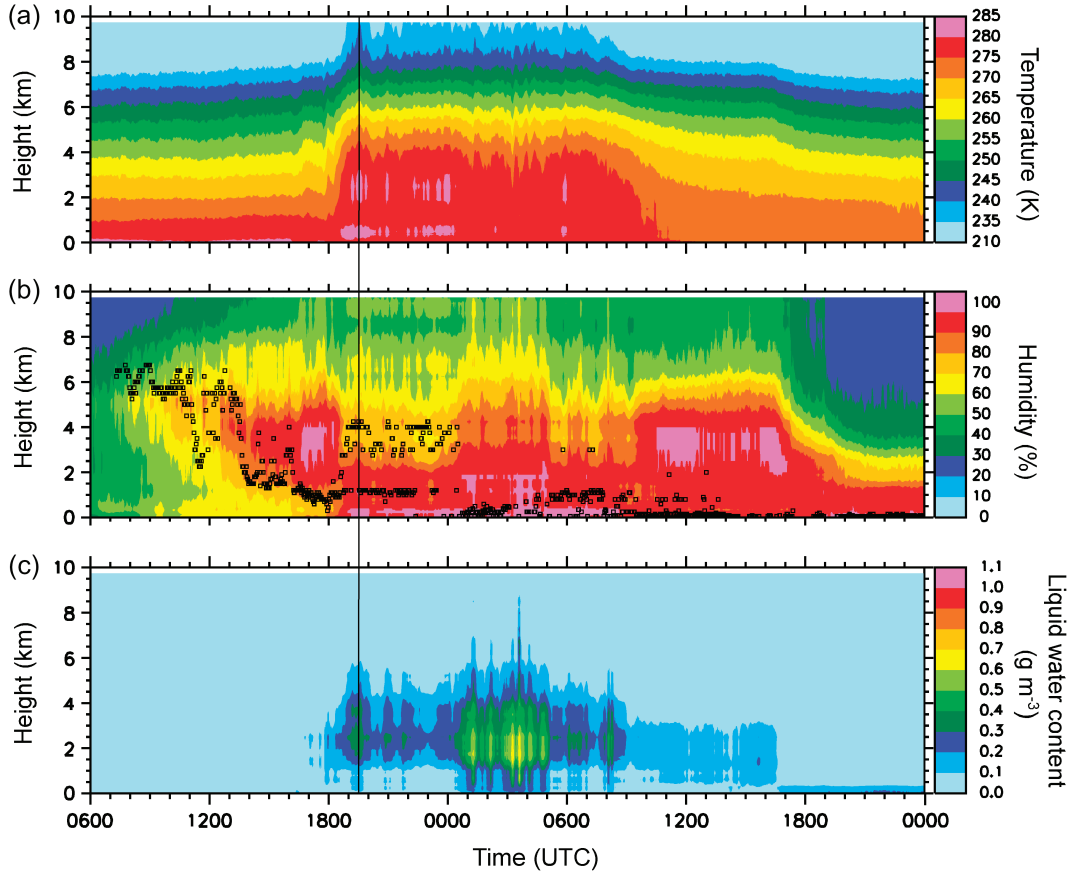

Figure 10. Time-height sections of (a) temperature (K), (b) RH (%) and (c) liquid water content (g m^{-3}) observed by the MWR from 0600 UTC on 26 February to 0000 UTC on 28 February. The symbols of square in (b) indicate cloud base heights measured by the MWR. The vertical line indicates the start time of rainfall as shown in Figure 8.

4. Summary and conclusions

The snow and rain events that brought light-to-moderate precipitation to the Seoul metropolitan area were observed by a microwave radiometer (MWR), radiosonde and a wind profiler during the winter of 2011. The temporal characteristics of temperatures and thicknesses, especially Z(1000–850), and the vertical structure were investigated in this study. It was found from the large curve shapes between Z(1000–850) and MWR precipitable water vapour (MPWV) that there were lead time periods of 9, 11 and 12 h showing little change in Z(1000–850) before precipitation against the continued increase in MPWV. The presence of the lead periods was also identified in the Z(1000–850) time series. This was possible because the MWR could detect a subtle thermal change associated with the approach of a mesoscale surface low pressure towards the Seoul area. Considering that

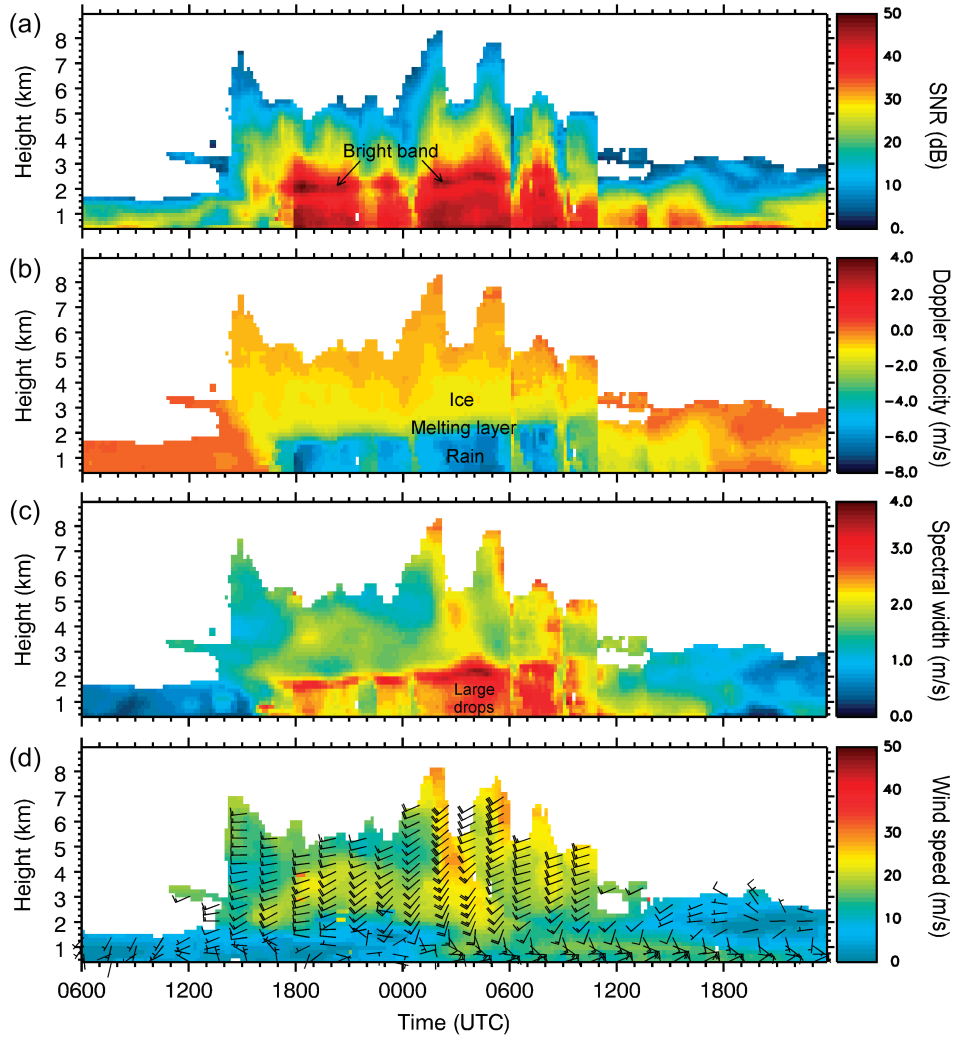

Figure 11. Time-height sections of (a) SNR (dB), (b) Doppler velocity (m s^{-1}) (negative downward), (c) spectral width (m s^{-1}) and (d) wind speed (m s^{-1}) observed by the wind profiler from 0600 UTC on 26 February to 2400 UTC on 27 February.

Z(1000–850) is proportional to the mean virtual temperature of the 1000–850 hPa layer, the MWR could observe the increase in low-level temperatures (below 850 hPa level) by warm air advection, leading to the increase in Z(1000–850). At certain times, however, the 1000 and 850 hPa levels started to change in a more parallel way with each other before precipitation. It is probably because warm air advection becomes relatively more neutral at low levels as the surface low pressure gets closer to the area.

As the lead periods are found in all the events analysed, thermodynamic properties at low levels (below the 850 hPa level) turn out to be similar between the snow and rain events in this study. However, the upper-level variations in thickness and temperature were different, depending on the vertical extent (i.e. cloud top height) of the systems. In this context, the approximate cloud top heights from the upper boundaries of the signal-to-noise ratio (SNR) minimum and 100% relative humidity (RH) could be estimated. It showed that the snow clouds are shallow with a top height of ~3 km AGL and the cloud top height is much higher at 7–8 km AGL for the rain event. Comparison between the MWR and radiosonde observations (RAOBs) showed that the correlation co-efficient was highest in the 1000–850 hPa layer and decreased with height. Such high correlations at low levels prove that the finding of the lead periods determined from the MWR-derived Z(1000–850) is reliable and meaningful in this study. Thus, for forecasting snowfall during wintertime, it is expected that MWR profiles at low levels can be more effectively used since the MWR can resolve low-level thermal structures more accurately at higher vertical resolutions.

The wind profiler observations of SNR, Doppler velocity, winds and so on were well matched with the MWR-observed properties although there was a spatial difference between the two sites. In the rain event, the surface R was higher under the raised, strong bright band. The MWR liquid water path (MLWP) was almost proportional to the surface R and the MPWV was more positively correlated with T700, T500 and Z(1000–500). For the weak, shallow snow systems, the MLWP and MPWV values were much smaller than those for the rain system with a deeper vertical extent. Above the melting level, there was a positive relation between winds and spectral widths in the ice regions. The low-level winds were weak and irregular during weak or no rainfall but showed a notable veer after rainfall gets stronger, associated with warm humid air advection by southerly and southwesterly winds.

Thus, the effectiveness of using the wind profiler as a complementary tool for the MWR is stressed upon in this study for analysing both the dynamic structure and related thermodynamic properties in the rain and ice regions, including a melting layer between. Also the MWR's ability to detect subtle thermodynamic

changes at low levels by continuous profiling, which is not possible with RAOBs, is highlighted in this study. Monitoring of the Z(1000–850) is particularly important for a snow or rain forecast precursor. With combined observations, more MWR studies need to be performed to analyse such low-level thickness properties to improve short-term forecasts as well as to verify the presence of the lead periods in similar cases over Korea.

Acknowledgements

The authors would like to thank the Forecast Research Division at the National Institute of Meteorological Research (NIMR), Korea, for providing all the data used in this study. This research was supported by the National Research Foundation of Korea (NRF) through a grant provided by the Korean Ministry of Education, Science & Technology (MEST) in 2014 (No. 200603874). This research was also partially supported by the Korea Meteorological Administration Research and Development Program under Grant CATER 2012–2071.

References

Bianco L, Cimini D, Marzano FS, Ware R. 2005. Combining microwave radiometer and wind profiler radar measurements for high-resolution atmospheric humidity profiling. *J. Atmos. Oceanic Technol.* **22**: 949–965.

Campos EF, Ware R, Joe P, Hudak D. 2014. Monitoring water phase dynamics in winter clouds. *Atmos. Res.* **147–148**: 86–100.

Chan PW. 2009. Performance and application of a multi-wavelength, ground-based microwave radiometer in intense convective weather. *Meteorol. Z.* **18**: 253–265.

Cimini D, Campos E, Ware R, Albers S, Graziano G, Oreamuno J, *et al.* 2011. Thermodynamic atmospheric profiling during the 2010 Winter Olympics using ground-based microwave radiometry. *IEEE Trans. Geosci. Remote Sens.* **49**: 4959–4969.

Cimini D, Nelson M, Güldner J, Ware R. 2014. Forecast indices from ground-based microwave radiometer for operational meteorology. *Atmos. Meas. Tech. Discuss.* **7**: 6971–7011.

Gaffard C, Nash J, Walker E, Hewison TJ, Jones J, Norton EG. 2008. High time resolution boundary layer description using combined remote sensing instruments. *Ann. Geophys.* **26**: 2597–2612.

Güldner J, Spänkuch D. 1999. Results of year-round remotely sensed integrated water vapor by ground-based microwave radiometry. *J. Appl. Meteorol.* **38**: 981–988.

Güldner J, Spänkuch D. 2001. Remote sensing of the thermodynamic state of the atmospheric boundary layer by ground-based microwave radiometry. *J. Atmos. Oceanic Technol.* **18**: 925–933.

Heppner POG. 1992. Snow versus rain: Looking beyond the "Magic" numbers. *Weather Forecast.* **7**: 683–691.

Keeter KK, Cline JW. 1991. The objective use of observed and forecast thickness values to predict precipitation type in North Carolina. *Weather Forecast.* **6**: 456–468.

Kneifel S, Lohnert U, Battaglia A, Crewell S, Siebler D. 2010. Snow scattering signals in ground-based passive microwave radiometer measurements. *J. Geophys. Res.* **115**: D16214, DOI: 10.1029/2010JD013856.

Knupp KR, Coleman T, Phillips D, Ware R, Cimini D, Vandenberghe F, *et al.* 2009. Ground-based passive microwave profiling during dynamic weather conditions. *J. Atmos. Oceanic Technol.* **26**: 1057–1073.

Liou YA, Teng YT, Hove TV, Liljegren JC. 2001. Comparison of precipitable water observations in the near tropics by GPS, microwave radiometer, and radiosondes. *J. Appl. Meteorol.* **40**: 5–15.

Liu GR, Liu CC, Kuo TH. 2001. Rainfall intensity estimation by ground-based dual-frequency microwave radiometers. *J. Appl. Meteorol.* **40**: 1035–1041.

Löhnert U, Crewell S, Simmer C. 2004. An integrated approach toward retrieving physically consistent profiles of temperature, humidity, and cloud liquid water. *J. Appl. Meteorol.* **43**: 1295–1307.

Löhnert U, Kneifel S, Battaglia A, Hagen M, Hirsch L, Crewell S. 2011. A multisensor approach toward a better understanding of snowfall microphysics: The TOSCA Project. *Bull. Am. Meteorol. Soc.* **92**: 613–628.

Löhnert U, Turner DD, Crewell S. 2009. Ground-based temperature and humidity profiling using spectral infrared and microwave observations. *Part I: Simulated retrieval performance in clear-sky conditions. J. Appl. Meteorol. Climatol.* **48**: 1017–1032.

MacDonald A, Xie Y, Ware R. 2002. Diagnosis of three-dimensional water vapor using a GPS network. *Mon. Weather Rev.* **130**: 386–397.

Madhulatha A, Rajeevan M, Venkat Ratnam M, Bhate J, Naidu CV. 2013. Nowcasting severe convective activity over southeast India using ground-based microwave radiometer observations. *J. Geophys. Res. Atmos.* **118**: 1–13, DOI: 10.1029/2012JD018174.

Massie DR, Rose MA. 1997. Predicting daily maximum temperatures using linear regression and Eta geopotential thickness forecasts. *Weather Forecast.* **12**: 799–807.

Serke D, Hall E, Bognar J, Jordan A, Abdo S, Baker K, *et al.* 2014. Supercooled liquid water content profiling case studies with a new vibrating wire sonde compared to ground-based microwave radiometer. *Atmos. Res.* **149**: 77–87.

Solheim F, Godwin J, Westwater E, Han Y, Keihm S, Marsh K, *et al.* 1998. Radiometric profiling of temperature, water vapor, and cloud liquid water using various inversion methods. *Radio Sci.* **33**: 393–404.

Spänkuch D, Guldner J, Steinhagen H, Bender M. 2011. Analysis of a dryline-like feature in northern Germany detected by ground-based microwave profiling. *Meteorol. Z.* **20**: 409–421.

Van Baelen J, Aubagnac JP, Dabas A. 2005. Comparison of near-real time estimates of integrated water vapor derived with GPS, radiosondes, and microwave radiometer. *J. Atmos. Oceanic Technol.* **22**: 201–210.

Venkat Ratnam M, Durga Santhi Y, Rajeevan M, Vijaya Bhaskara Rao S. 2013. Diurnal variability of stability indices observed using radiosonde observations over a tropical station: comparison with microwave radiometer measurements. *Atmos. Res.* **124**: 21–33.

Ware R, Cimini D, Campos E, Giuliani G, Albers S, Nelson M, *et al.* 2013. Thermodynamic and liquid profiling during the 2010 Winter Olympics. *Atmos. Res.* **132–133**: 278–290.

Westwater ER, Decker MT, Zachs A, Gage KS. 1983. Ground-based remote sensing of temperature profiles by a combination of microwave radiometry and radar. *J. Clim. Appl. Meteorol.* **22**: 126–133.

Westwater ER, Stankov BB, Cimini D, Han Y, Shaw JA, Lesht BM, *et al.* 2003. Radiosonde humidity soundings and microwave radiometers during Nauru99. *J. Atmos. Oceanic Technol.* **20**: 953–971.

Xu G, Ware RS, Zhang W, Feng G, Liao K, Liu Y. 2014. Effect of off-zenith observations on reducing the impact of precipitation on ground-based microwave radiometer measurement accuracy. *Atmos. Res.* **140–141**: 85–94.

